Version of Record: https://www.sciencedirect.com/science/article/pii/S2095927323003821
Manuscript_c6f3a1a00cea737d369deef114cc0a15

Article

The stability of FeH_x and hydrogen transport at Earth's core mantle boundary

Yu He[a,b], Duck Young Kim[b,c,*], Viktor V. Struzhkin[b], Zachary M. Geballe[d], Vitali Prakapenka[e], Ho-kwang Mao[b]

[a]Key Laboratory of High-Temperature and High-Pressure Study of the Earth's Interior, Institute of Geochemistry, Chinese Academy of Sciences, Guiyang 550081, China.

[b]Center for High Pressure Science and Technology Advanced Research, Shanghai 201203, China

[c]Division of Advanced Nuclear Engineering, Pohang University of Science and Technology, Pohang 37673, Republic of Korea

[d]Geophysical Laboratory, Carnegie Institution, Washington, DC 20015, USA

[e]Center for Advanced Radiation Sources, University of Chicago, Chicago, IL 60637, USA

*Corresponding author: Duck Young Kim, **E-mail:** duckyoung.kim@hpstar.ac.cn

Received 04 August, 2022 ; Revised 29 May, 2023 ; Accepted 31 May, 2023

ABSTRACT

Iron hydride in Earth's interior can be formed by the reaction between hydrous minerals (water) and iron. Studying iron hydride improves our understanding of hydrogen transportation in Earth's interior. Our high-pressure experiments found that face-centered cubic (fcc) FeH_x ($x \leq 1$) is stable up to 165 GPa, and our *ab initio* molecular dynamics simulations predicted that fcc FeH_x transforms to a superionic state under lower mantle conditions. In the superionic state, H-ions in fcc FeH become highly diffusive-like fluids with a high diffusion coefficient of ~3.7×10^{-4} cm^2 s^{-1}, which is comparable to that in the liquid Fe-H phase. The densities and melting temperatures of fcc FeH_x were systematically calculated. Similar to superionic ice, the extra entropy of diffusive H-ions increases the melting temperature of fcc FeH. The wide stability field of fcc FeH enables hydrogen transport into the outer core to create a potential hydrogen reservoir in Earth's interior, leaving oxygen-rich patches (ORP) above the core mantle boundary (CMB).

Keywords: iron hydride; hydrogen transportation; Superionic; Earth's interior; core-mantle boundary

1. Introduction

Hydrogen is one of the most important volatiles on Earth. It forms water that covers 70% of Earth's surface and is a unique biochemical ingredient that makes Earth a living planet. In Earth's interior, hydrogen is usually correlated with oxygen and is present in the hydroxyl groups of hydrous minerals and nominally anhydrous minerals. Hydrogen transport in Earth's interior is a long-standing research subject [1-5]. Trace amounts of hydrogen can significantly influence the properties of minerals, such as density, seismic velocity, electrical conductivity, and rheology [4,5]. In addition, hydrogen is one of the light elements present in Earth's core, affecting its density, seismic velocity, temperature profile, and thermal conduction [6-15]. Hydrogen in the core may originate directly from the protosolar nebula during the formation of Earth [16,17]. Alternatively, it is brought down to the core mantle boundary (CMB) by ultra-dense hydrous phases including δ-AlOOH [18,19], phase H [20], ε-FeOOH [21,22] pyrite FeO_2H [23-25], and hydrous aluminium magnesium silicates [26,27]. The H_2O released from these hydrous minerals can react with iron at the CMB. The reaction between Fe and H_2O has been extensively studied at high pressures [1,28-30]. At pressures below 70 GPa,

$$Fe+H_2O \rightarrow FeO + FeH_x \qquad (1).$$

Because of this reaction, Fe-H alloys were formed by the reaction between iron and hydrous magma of the early Earth [6,16]. Alternatively, Fe-H alloys are generated in the mantle through the reaction between disproportionated metallic Fe [31-33] and water released from subducted slabs and/or hydrous minerals [34].

The chemical reaction between water and iron is different above 80 GPa [23],

$$Fe+H_2O \rightarrow FeO_2H_x + FeH_x \qquad (2).$$

At the CMB, water can be released from hydrous minerals and react with Fe from the outer core to generate pyrite, FeO_2H_x, and FeH_x. Pyrite FeO_2H_x exhibits significantly lower seismic velocities than the

Preliminary Reference Earth Model (PREM) data [35]. Thus, the presence of this phase in the lowermost mantle accounts for the low seismic velocities observed in the ultralow velocity zone (ULVZ) [36]. However, the properties of FeH_x under CMB conditions are important for establishing hydrogen transport in Earth's interior.

At ambient pressure, iron does not form compounds with hydrogen. At high pressure, the solubility of H_2 in Fe increases dramatically to form various Fe-H phases [7-10, 37-39]. Among these phases, double hexagonal close-packed (dhcp) FeH_x ($x \leq 1$) and fcc FeH_x ($x \leq 1$) are considered two stable crystal structures under the conditions of Earth's interior [37-40]. fcc FeH_x is computationally predicted to be more stable at pressures and temperatures above ~80 GPa and 300 K, respectively [40]. Experimental studies have also documented the stability of the fcc FeH_x phase at pressures and temperatures up to ~140 GPa and 3500 K, respectively [41-45]. Here, we calculated the stability, densities, and melting temperatures of fcc FeH_x (x = 1, 0.5) alloys using *ab initio* molecular dynamics (AIMD) simulations. We will discuss the influence of fcc FeH_x on hydrogen transportation from the mantle to the core based on the calculated results.

2. Methods

The experiments were performed in a symmetric diamond anvil cell (DAC) [46]. X-ray diffraction measurements and online laser heating were performed at Sector 13 (GSECARS), Advanced Photon Source, Argonne National Laboratory [47]. The sample was heated slightly by an infrared laser online at several pressures above 60 GPa so that no thermal radiation was detected during heating. We performed density functional theory (DFT) calculations using the Vienna *Ab Inito* Simulation Package (VASP) [48]. We used atomic potentials generated using the projector augmented-wave method (PAW) [49] within the generalised gradient approximations (GGA). The migration path and energy barrier of the H-ion were calculated using the climbing-image nudged elastic band (CINEB) method [50]. We performed AIMD simulations using 3 × 3 × 3 supercells, which contained 216 atoms for FeH and 162 atoms for $FeH_{0.5}$. The

simulations used the canonical ensemble with a time step of 1 fs, with the simulations lasting 15 ps at temperatures ranging from ~1000–4000 K. We calculated the diffusion coefficient for H-ion transport and the mean square displacement (MSD) of the ionic positions. The melting temperature was estimated using the two-phase method. The AIMD simulation was conducted on the solid-liquid coexistence model containing 432 atoms for FeH and 324 atoms for $FeH_{0.5}$ in the *NPT* (*N*, number of particles; *P*, pressure; *T*, temperature) ensemble, in which the number of atoms, pressure, and temperature are constants. Detailed methods are provided in the Supplementary materials (online).

3. Results

In this study, *in situ* X-ray diffraction (XRD) measurements were performed with Fe starting material in a hydrogen medium at pressures up to 165 GPa at 190 K. The fcc FeH_x ($x \leq 1$) phase was observed starting at 60 GPa and remained stable during compression to 165 GPa and decompression to nearly 10 GPa. The XRD patterns and pressure-volume (*P-V*) relationships are shown in Figs. S1–S3 (online). Our high-pressure experimental results suggest that fcc FeH_x can be a stable phase, at least up to the pressure of the outer core, which is consistent with previous theoretical predictions [40]. High-pressure experiments suggest that fcc FeH_x is stable at temperatures up to ~3600 K and pressures up to ~140 GPa [44,45]. Considering the wide stability field of fcc FeH_x in the *P-V* phase diagram, we conducted *ab initio* calculations to study the properties of fcc FeH_x under the conditions of the lowermost mantle and uppermost core.

We calculated the migration paths and barrier energies of the H-ions with increasing pressure (Fig. 1a, b). Fig. 1 shows that the octahedral-tetrahedral-octahedral (O-T-O) path is more favourable owing to its lower energy barrier compared to the direct octahedral-octahedral (O-O) path. We further performed AIMD simulations on fcc FeH_x (x = 1 and 0.5) within the temperature and pressure ranges of 1000–4000 K and 40–180 GPa. At 1000 K, the H-ions vibrating in their lattice positions behaved like normal solids. With increasing temperature, H-ions started to diffuse in the Fe sublattice, and the MSD increased significantly with simulation time, indicating a superionic state (Fig. 1c and Fig. S4 online). The superionic state

exhibits partial melting of solids while the original structure is maintained; thus, it is located between the solid and liquid phases. Superionicity was predicted to exist under Earth's inner core conditions [14,15,52] and was experimentally observed in ice at the exoplanets' interior [53] and in FeO_2H_x at Earth's CMB [54]. We calculated that fcc FeH_x was in a superionic state at lower mantle pressure and temperature (Fig. 1d, e). The superionic transition temperature of FeH is higher than that of $FeH_{0.5}$ by ~500 K owing to the presence of more hydrogen vacancies in the lattice, which enhances H-ion diffusion by providing more migration sites.

The H-ion diffusion coefficients were deduced from the MSDs of the H-ions in the superionic state (Fig. 2). The calculated diffusion coefficients at high *P-T* were fitted using the Arrhenius equation, and the activation enthalpies for H-ion diffusion were calculated. The energy barrier of H-ion diffusion in fcc FeH is approximately 0.5 eV higher than the activation enthalpy for H-ion diffusion in $FeH_{0.5}$ due to the effect of hydrogen vacancies, as mentioned above. Under CMB conditions, the H-ion diffusion coefficients ranged from ~1.8×10^{-4} to 3.2×10^{-5} cm^2 s^{-1}. These values are very close to the ionic diffusion coefficients of superionic FeO_2H (blue region in Fig. 2) [54]. However, the superionic transition temperature of FeO_2H is approximately 500 K higher than that of fcc FeH_x. We also estimated the superionic transition temperatures using the extrapolated diffusion coefficients. According to the Li^+ diffusion coefficients of the typical superionic material Li_2O [55], the transition temperatures for diffusion coefficients larger than 10^{-6} cm^2 s^{-1} were deduced and are shown as orange stars in Fig. 1d, e.

The H-ion in fcc FeH takes $-0.26e$ based on the estimation from the Bader charge analysis method (Table S1 online), and this value does not change with pressure. The ionic conductivities were calculated based on this value (Fig. S5 online). The H-ion conductivities of fcc FeH and $FeH_{0.5}$ under CMB conditions, are in the range of ~16-100 S m^{-1}. The reported conductivity of fcc FeH_x is ~2.4×10^6 S m^{-1} at ~65 GPa and ~1700 K [56], which is much higher than the H-ion conductivity.

Based on the calculated volume using AIMD simulations, the *P-V* relationships of FeH_x at different temperatures were obtained and fitted with the equation of states (Fig. S3 online). The results are consistent with the experimental results at 190 and 300 K [42,44] at pressures over 80 GPa (Fig. S3a online). At low pressures, the calculated volumes are underestimated owing to the strongly correlated d electrons of Fe. This discrepancy can be minimised by adopting a proper Hubbard U correction [57]. At elevated temperatures, the calculated volumes were approximately 4% larger than the experimental volume [44]. Using the *P-V* relationships of FeH and $FeH_{0.5}$, the volume change (ΔV_H) due to hydrogen incorporation was estimated (Fig. S6 online). Here, the densities of fcc FeH_x (x =1 and 0.5) under CMB conditions were calculated (Fig. 3). We also evaluated the density of fcc $FeH_{0.75}$ by averaging the densities of FeH and $FeH_{0.5}$. In comparison with geophysical observations, fcc $FeH_{0.75}$ is less dense than the outer core. According to our calculated densities of the liquid Fe-H alloy (Fig. S7 online), the estimated hydrogen concentration should be less than 1.1 wt% to fit the density of the uppermost outer core.

The liquid state is obtained when the temperature is increased to over 3500 K. The MSDs of both H and Fe increase with the simulation time in the liquid phase. However, the temperatures obtained in the single-phase AIMD simulation could be several hundred degrees higher than the true melting temperature owing to the superheating solid-state [58]. The melting temperature is important for understanding the thermal stability of fcc FeH_x under CMB conditions. Moreover, this value can be used to estimate the temperature profile of the outer core considering the presence of hydrogen. In our study, the melting temperature of fcc FeH was calculated more accurately using a two-phase method [59]. In the two-phase method, both the solid and liquid phases coexist in the starting model. After several picoseconds of AIMD simulations at different temperatures, either a pure liquid or solid phase was obtained (Figs. S8 and S9 online). The solidus phase maintained the fcc structure (Fig. S10 online), and the calculated melting temperatures for fcc FeH and $FeH_{0.5}$ are 2721 (±40) and 3005 (±40) K, respectively. The estimated melting temperature was approximately 300 K higher than the extrapolated melting curve of fcc FeH at pressures lower than 20 GPa (Fig. 4) [12]. It has been reported that the melting temperature of superionic ice increases owing to the extra entropy of disordered H-ions [53]. It is likely that the same effect increases the melting temperature of

fcc FeH. However, the melting temperature is approximately 1000 K lower than recent measurements on stoichiometric FeH above 120 GPa. The higher melting temperatures of FeH at high pressures were attributed to the magnetic to nonmagnetic (NM) transition [45]. We will discuss the possible reasons for these discrepancies of volumes and melting temperatures in the discussion section. In the two-phase simulations, we observed the diffusion of H-ions across the solid–liquid boundary, as shown in the trajectory of H-ions (Fig. 5) in the two-phase simulation. In the superionic state, although the Fe sublattice still maintains an ordered periodic structure, liquid-like H-ions are free to diffuse into the liquid phase.

4. Discussion

The fate of FeH_x at the CMB depends on its density and stability. The calculated volumes show consistency at 300 K, but the discrepancy increases to 4% at temperatures over 1500 K, and the calculated different volumes of hydrogen (ΔV_H) have an opposite trend compared to the experimental study (Fig. S6 online) [44]. It suggests that the temperature effect is critical for these discrepancies. In particular, the calculated melting temperature was approximately 1000 K lower than the experimental results. Here, we used a relatively small model that did not consider the presence of Fe vacancies and grain boundaries. It is known that the concentration of Schottky defects increases dramatically with increasing temperature, and the defect concentration is higher at the grain boundaries. Based on simulations of the model with Fe vacancies, the vacancy sites accommodate extra hydrogen owing to this superionic behaviour (Fig. S11 online). Thus, the hydrogen concentration in the bulk material should be lower owing to the presence of defects. In addition, the temperature gradient and/or differential stress may cause inhomogeneous hydrogen concentrations in the sample. In principle, distinguishing the discrepancy between the experiments and simulations can be helpful in understanding the distinctive superionic behaviour of FeH_x.

FeH is synthesised from water and iron reactions at high *P-T*. Water exists in the form of hydrous minerals in Earth's interior, which can be brought down to the deep Earth through subduction process. Water released from subduction slabs due to the dehydration of hydrous minerals can react with metallic iron in

the mantle (Fig. 6). Generally, the dominant redox state of Fe in the mantle is Fe^{2+}. However, because of the disproportionation of Fe^{2+}, metallic Fe alloys are synthesised under mantle conditions [31]. Recently, liquid Fe alloys were found in diamonds from the lower mantle, providing direct evidence of the existence of metallic Fe and metal-saturated regions in the deep mantle [33]. The estimated metallic Fe content is ~1 wt% at the top of the lower mantle [31,32]. In the presence of water (hydrous minerals) and metallic Fe, FeH can be formed and transported to the deepest mantle by mantle convection. On the other hand, water can be brought to the deepest lower mantle by ultra-dense hydrous phases [29,68]. Thus, FeH can be produced by the reaction of the released water and Fe from the core (Eq. (2)). This process also generates significant amounts of FeO_2 and FeO_2H_x, which are less dense than FeH and can be deposited as oxygen-rich patches (ORP) above the CMB. The accumulation of the ORP provides an explanation for the formation of the ULVZ, and the eruption of the ORP may have impacted the Great Oxidation Event [29,69].

Superionic fcc FeH_x is stable under the conditions of the lowermost mantle and D″ layer (the lowermost portion of the mantle). The geotherm increases rapidly to over 3000 K in the D″ layer and further increases to the temperature of the CMB (T_{CMB}). The T_{CMB} was determined by adiabatic extrapolation from the melting temperature of the Fe alloy at the inner core boundary (P_{ICB} = 330 GPa). However, a large deviation existed in the measurements of the melting temperature of pure Fe. The gap between the high and low melting curves of Fe is ~500–700 K [60-64]. Thus, the predicted T_{CMB} also presents significant uncertainty, as indicated by the red and blue updown arrows in Fig. 4. The presence of nickel and light elements (S, O, and Si) in the outer core can lower the T_{CMB} to approximately 3500 K (green arrow in Fig. 4) [62]. The T_{CMB} may be even lower (~3100–3570 K), as predicted from the solidus temperature of pyrolite (yellow arrow in Fig. 4) [67]. The melting temperature of fcc FeH_x is critical. If it is higher than 3500 K, as suggested by the experimental study [45], fcc FeH_x with x > ~0.75 is less dense than the outer core and may float above the topmost outer core, adopting the low T_{CMB} prediction. The deposition of fcc FeH_x alloy at the CMB with high conductivities can offer a plausible explanation for the electromagnetic (EM) coupling between the liquid core and solid mantle, which may affect Earth's nutation and cause a change in the length of day [70]. Alternatively, fcc FeH_x eventually melts into the outer core with a rapid

increase in temperature at the CMB. Thus, hydrogen in the form of water at Earth's surface is transported down to the core in the form of an Fe-H alloy. Considering the strong partitioning of hydrogen into liquid Fe over silicate melt [71-73], the core should be a reservoir of hydrogen in the deep Earth. Hydrogen in the outer core affects the density, temperature profile, seismic velocity, and thermal conductivity of the core. The hydrogen concentration in the outer core was estimated to be ~0.5 wt%–2 wt% in previous experimental and computational studies by comparing the material properties with the density and seismic velocity of the outer core [10,12,74]. Our study shows that ~1.1 wt% hydrogen in a liquid Fe-H alloy can fit the density of the outer core. Considering the presence of other light elements (S, Si, O, and C) in the outer core, the hydrogen content should be lower. Further constraining the composition and content of the light elements will benefit our understanding of the state and history of the outer core.

Conflict of interest

The authors declare that they have no conflict of interest.

Acknowledgments

This work was supported by the National Natural Science Foundation of China (42074104, 11774015, and U1930401), Youth Interdisciplinary Team of Chinese Academy of Sciences (JCTD-2022-16), Youth Innovation Promotion Association of Chinese Academy of Sciences (2020394), and Guizhou Provincial 2020 Science and Technology Subsidies (GZ2020SIG). Duck Young Kim also acknowledges the support from the National Research Foundation of Korea (NRF-2020R1A2C1005236). Portions of this work were performed at GeoSoilEnviroCARS (the University of Chicago, Sector 13), Advanced Photon Source (APS), Argonne National Laboratory. GeoSoilEnviroCARS is supported by the National Science Foundation—Earth Sciences (EAR-1634415). This work used resources from the APS, a U.S. Department of Energy (DOE) Office of Science User Facility operated for the DOE Office of Science by Argonne National Laboratory under Contract No. DE-AC02-06CH11357. Numerical computations were performed at Hefei Advanced Computing Center, Shanghai Supercomputer Center, and National Supercomputer Center in Guangzhou.

Author contributions

Yu He, Duck Young Kim, and Ho-kwang Mao designed the study. Yu He performed calculations. Viktor V. Struzhkinb, Zachary M. Geballec, and Vitali Prakapenka conducted high-pressure experiments. All the authors discussed the results and contributed to the writing of the paper.

References

[1] Ni H, Zheng Y-F, Mao Z, et al. Distribution, cycling and impact of water in the Earth's interior. Natl Sci Rev 2017;4:879-91.

[2] Mao H-K, Mao, WL. Key problems of the four-dimensional Earth system. Matter Radiat Extremes 2020;5:038102.

[3] Ohtani E. Hydration and dehydration in Earth's interior. Annu Rev Earth Planet Sci 2021;49:253–78.

[4] Ohtani E. The role of water in Earth's mantle. Natl Sci Rev 2020;7:224-32.

[5] Walter M. Water transport to the core–mantle boundary. Natl Sci Rev 2021;8:nwab007.

[6] Okuchi T. Hydrogen partitioning into molten iron at high pressure: implications for Earth's core. Science 1997;278:1781-1784.

[7] Hirao N, Kondo T, Ohtani E, et al. Compression of iron hydride to 80 GPa and hydrogen in the Earth's inner core. Geophys Res Lett 2004;31:L06616.

[8] Sakamaki K, Takahashi E, Nakajima, Y, et al. Melting phase relation of FeH_x up to 20 GPa: implication for the temperature of the Earth's core. Phys Earth Planet Inter 2009;174:192-201.

[9] Narygina O, Dubrovinsky LS, McCammon CA, et al. X-ray diffraction and Mössbauer spectroscopy study of fcc iron hydride FeH at high pressures and implications for the composition of the Earth's core. Earth Planet Sci Lett 2011;307:409-414.

[10] Shibazaki Y, Ohtani E, Fukui H, et al. Sound velocity measurements in dhcp-FeH up to 70 GPa with inelastic X-ray scattering: implications for the composition of the Earth's core. Earth Planet Sci Lett 2012;313-314:79-85.

[11] Caracas R. The influence of hydrogen on the seismic properties of solid iron. Geophys Res Lett 2015;42:3780-3785.

[12] Umemoto K, Hirose K. Liquid iron-hydrogen alloys at outer core conditions by first-principles calculations. Geophys Res Lett 2015;42:7513-7520.

[13] Gomi H, Fei Y, Yoshino T. The effects of ferromagnetism and interstitial hydrogen on the equation of states of hcp and dhcp FeH_x: implications for the Earth's inner core age. Am Miner 2018;103:1271-81.

[14] He Y, Sun S, Kim DY et al. Superionic hcp-Fe alloys and their seismic velocities in Earth's inner core. Nature 2022;602:258–262.

[15] Wang W, Li Y, Brodholt JP, et al. Strong shear softening induced by superionic hydrogen in Earth's inner core. Earth Planet Sci Lett 2021;568:117014.

[16] lizuka-Oku R, Yagi T, Gotou H, et al. Hydrogenation of iron in the early stage of Earth's evolution. Nat Commun 2017;8:14096.

[17] Hallis LJ, Huss GR, Nagashima K, et al. Evidence for primordial water in Earth's deep mantle. Science 2015;350:795-797.

[18] Sano A, Ohtani E, Kondo T, et al. Aluminous hydrous mineral δ-AlOOH as a carrier of hydrogen into the core-mantle boundary. Geophys Res Lett 2008;35:L03303.

[19] Duan Y, Sun N, Wang S, et al. Phase stability and thermal equation of state of δ-AlOOH: implication for water transportation to the deep lower mantle. Earth Planet Sci Lett 2018;494:92-98.

[20] Nishi M, Irifune T, Tsuchiya J, et al. Stability of hydrous silicate at high pressures and water transport to the deep lower mantle. Nat Geosci 2014;7:224-227.

[21] Gleason AE, Quiroga CE, Suzuki A, et al. Symmetrization driven spin transition in ε-FeOOH at high pressure. Earth Planet Sci Lett 2013;379:49–55.

[22] Zhuang Y, Gan B, Cui Z, et al. Mid-mantle water transportation implied by the electrical and seismic properties of e-FeOOH. Sci Bull 2022;67:748-754.

[23] Hu Q, Kim DY, Liu J, et al. Dehydrogenation of goethite in Earth's deep lower mantle. Proc Natl Acad Sci USA 2017;114:1498–501.

[24] Nishi M, Kuwayama K, Tsuchiya J, et al. pyrite-type high-pressure form of FeOOH. Nature 2017;547:205–208.

[25] Tang R, Liu J, Kim DY, et al. Chemistry and *P-V-T* equation of state of FeO_2H_x at the base of Earth's lower mantle and their geophysical implications. Sci Bull 2021;66:1954-1958.

[26] Ohira I, Ohtani E, Sakai T, et al. Stability of a hydrous δ-phase, $AlOOH\text{-}MgSiO_2(OH)_2$, and a mechanism for water transport into the base of lower mantle. Earth Planet Sci Lett 2014;401:12-17.

[27] Pamato MG, Myhill R, Ballaran TB, et al. Lower-mantle water reservoir implied by the extreme stability of a hydrous aluminosilicate. Nat Geosci 2015; 8: 75-79.

[28] Fukai Y. The iron–water reaction and the evolution of the Earth. Nature 1984;308:174–5.

[29] Mao H-K, Hu Q, Yang L, et al. When water meets iron at Earth's core-mantle boundary. Natl Sci Rev 2017;4:870-878.

[30] Yuan L, Ohtani E, Ikuta D, et al. Chemical reactions between Fe and H_2O up to megabar pressures and implications for water storage in the Earth's mantle and core. Geophys Res Lett 2018;45:1330–38.

[31] Frost DJ, Liebske C, Langenhorst F, et al. Experimental evidence for the existence of iron-rich metal in the Earth's lower mantle. Nature 2004;428:409-412.

[32] Frost DJ, McCammon CA. The redox state of Earth's mantle. Annu Rev Earth Planet Sci 2008;36:389–420.

[33] Smith EM, Shirey SB, Nestola F, et al. Large gem diamonds from metallic liquid in Earth's deep mantle. Science 2016;354:1403-1405.

[34] Zhu F, Li J, Liu J, et al. Metallic iron limits silicate hydration in Earth's transition zone. Proc Natl Acad Sci USA 2019;116:22526-22530.

[35] Dziewonski AM, Anderson DL. Preliminary reference Earth model. Phys Earth Planet Inter 1981;25:297-356.

[36] Liu J, Hu Q, Kim DY, et al. Hydrogen-bearing iron peroxide and the origin of ultralow-velocity zones. Nature 2017;551:494-497.

[37] Badding JV, Hemley RJ, Mao H-K, et al. High-pressure chemistry of hydrogen in metals: *in situ* study of iron hydride. Science 1991;253:421-424.

[38] Machida A, Saitoh H, Sugimoto H, et al. Site occupancy of interstitial deuterium atoms in face-centred cubic iron. Nat Commun 2014;5:5063.

[39] Pépin CM, Dewaele A, Geneste GP, et al. New iron hydrides under high pressure. Phys Rev Lett 2014;113:265504.

[40] Isaev EI, Skorodumova NV, Ahuja R, et al. Dynamical stability of Fe-H in the Earth's mantle and core regions. Proc Natl Acad Sci USA 2007;104:9168–71.

[41] Thompson EC, Davis AH, Bi W, et al. High-pressure geophysical properties of fcc phase FeH_X. Geochem Geophys Geosyst 2018;19:305-314.

[42] Kato C, Umemoto K, Ohta K, et al. Stability of fcc phase FeH to 137 GPa. Am Miner 2020;105:917-921.

[43] Ikuta D, Ohtani E, Sano-Furukawa A, et al. Interstitial hydrogen atoms in face-centered cubic iron in the Earth's core. Sci Rep 2019;9:7108.

[44] Tagawa S, Gomi H, Hirose K, et al. High-temperature equation of state of FeH: implications for hydrogen in Earth's inner core. Geophys Res Lett 2022;49:e2021GL096260.

[45] Tagawa S, Helffrich G, Hirose K, et al. High-pressure melting curve of FeH: implications for eutectic melting between Fe and non-magnetic FeH. J Geophys Res: Solid Earth 2022;127:e2022JB024365.

[46] Mao H-K, Shen G, Hemley RJ, et al. X-ray diffraction with a double hot-plate laser-heated diamond cell. In: Manghnani M H, Yagi T, editors. Properties of Earth and planetary materials at high pressure and temperature. American Geophysical Union: Washington DC, 1998, 101: 27-34.

[47] Prakapenka VB, Kubo A, Kuznetsov A, et al. Advanced flat top laser heating system for high pressure research at GSECARS: application to the melting behavior of germanium. High Press Res 2008;28:225–235.

[48] Kresse G. Efficient iterative schemes for *ab initio* total-energy calculations using a plane-wave basis set. Phys Rev B 1996;54:11169–86.

[49] Blöchl PE. Projector augmented-wave method. Phys Rev B 1994;50:17953–79.

[50] Henkelman G, Uberuaga BP, Jonsson H. A climbing image nudged elastic band method for finding saddle points and minimum energy paths. J Chem Phys 2000;113:9901–04.

[51] Brown JM, Shankland TJ. Thermodynamic parameters in the Earth as determined from seismic profiles. Geophys J Roy Astron Soc 1981;66:579–96.

[52] Sun S, He Y, Yang J, et al. Superionic effect and anisotropic texture in Earth's inner core driven by geomagnetic field. Nat Commun 2023;14:1656.

[53] Millot M, Coppari F, Rygg JR, et al. Nanosecond X-ray diffraction of shock-compressed superionic water ice. Nature 2019;569:251.

[54] Hou M, He Y, Jang BG, et al. Superionic iron oxide-hydroxide in Earth's deep mantle. Nat Geosci 2021;14:174-178.

[55] Oishi Y, Kamei Y, Akiyama M, et al. Self-diffusion coefficient of lithium in lithium oxide. J Nucl Mater 1979;87:341.

[56] Ohta K, Suehiro S, Hirose K, et al. Electrical resistivity of fcc phase iron hydrides at high pressures and temperatures. C R Geosci 2019;351:147-53.

[57] Liechtenstein AI, Anisimov VI, Zaanen J. Density-functional theory and strong interactions: orbital ordering in Mott-Hubbard insulators. Phys Rev B 1995;52:R5467.

[58] Belonoshko AB, Skorodumova NV, Rosengren A, et al. Melting and critical superheating. Phys Rev B 2006;73:012201.

[59] Belonoshko AB. Molecular dynamics of $MgSiO_3$ perovskite at high pressures: equation of state, structure, and melting transition. Geochim Cosmochim Acta 1994;58:4039-4047.

[60] Anzellini S, Dewaele A, Mezouar M, et al. Melting of iron at Earth's inner core boundary based on fast X-ray diffraction. Science 2013;340:464–6.

[61] Sinmyo R, Hirose K, Ohishi Y. Melting curve of iron to 290 GPa determined in a resistance-heated diamond-anvil cell. Earth Plant Sci Lett 2019;510:45-52.

[62] Zhang D, Jackson JM, Zhao J, et al. Temperature of Earth's core constrained from melting of Fe and $Fe_{0.9}Ni_{0.1}$ at high pressures. Earth Plant Sci Lett 2016;337:72-83.

[63] Li J, Wu Q, Li J, et al. Shock melting curve of iron: a consensus on the temperature at the Earth's inner core boundary. Geophys Res Lett 2020;47:e2020GL087758.

[64] Hou H, Liu J, Zhang Y, et al. Melting of iron explored by electrical resistance jump up to 135 GPa. Geophys Res Lett 2021;48:e2021GL095739.

[65] Morard G, Andrault D, Antonangeli D, et al. Fe−FeO and Fe‐Fe_3C melting relations at Earth's core–mantle boundary conditions: implications for a volatile‐rich or oxygen-rich core. Earth Plant Sci Lett 2017;473:94–103.

[66] Mori Y, Ozawa H, Hirose K, et al. Melting experiments on Fe–Fe_3S system to 254 GPa. Earth Plant Sci Lett 2017;464:135–141.

[67] Nomura R, Hirose K, Uesugi K, et al. Low core-mantle boundary temperature inferred from the solidus of pyrolite. Science 2014;343:522-525.

[68] Hu Q, Liu J, Chen J, et al. Mineralogy of the deep lower mantle in the presence of H_2O. Natl Sci Rev 2020;8:nwaa098.

[69] Hu Q, Kim DY, Yang W, et al. FeO_2 and FeOOH under deep lower-mantle conditions and Earth's oxygen–hydrogen cycles. Nature 2016;534:241-244.

[70] Mathews PM, Shapiro II. Nutations of the Earth. Annu Rev Earth Planet Sci 1992;20:469.

[71] Li Y, Vočadlo L, Sun T, et al. The Earth's core as a reservoir of water. Nat Geosci 2020;13:453–8.

[72] Yuan L, Steinle-Neumann G. Strong sequestration of hydrogen into the Earth's core during planetary differentiation. Geophys Res Lett 2020;47:e2020GL088303.

[73] Tagawa S, Sakamoto N, Hirose K, et al. Experimental evidence for hydrogen incorporation into Earth's core. Nat Commun 2021;12:2588.

[74] Terasaki H, Ohtani E, Sakai T, et al. Stability of Fe-Ni hydride after the reaction between Fe-Ni alloy and hydrous phase (δ-AlOOH) up to 1.2 Mbar: possibility of H contribution to the core density deficit. Phys Earth Planet Inter 2012;194-195:18–24.

Figure captions:

Fig. 1. H-ion transportation properties and high pressure–temperature phase diagrams of fcc FeH_x (x = 1 and 0.5). (a) Direct O-O (green) and indirect O-T-O (magenta) migration paths for H-ion migration in fcc FeH. (b) The calculated H-ion migration barrier energies with increasing pressure. (c) The trajectory of H-ions in solid and superionic FeH is shown with magenta spheres. The solid Fe sublattice is shown with brown spheres. (d), (e) Solid-superionic-liquid phase transition in fcc FeH_x (x = 1 and 0.5) at 1000–4000 K and 40–180 GPa. The blue, green, and red regions indicate the solid, superionic, and liquid states, respectively. The gray region represents uncertainty for the state transition. The estimated superionic transition temperatures based on the calculated diffusion coefficients are shown with orange stars. The geotherm for the mantle is shown with thick black solid curves [51].

Fig. 2. Calculated H-ion diffusion coefficients in fcc FeH (a) and $FeH_{0.5}$ (b). The calculated diffusion coefficients at 70–160 GPa are shown with different symbols. The values change with increasing temperature and are fitted to an Arrhenius equation with diffusion activation enthalpies noted in the figures. The diffusion coefficients of H-ions in superionic pyrite FeO_2H_x (x < 1) [54] are shown with blue regions. The dashed lines represent the diffusion coefficient for the superionic state, and the corresponding temperatures are the temperature for the solid-superionic transition.

Fig. 3. Calculated densities of FeH_x (x = 1, 0.75, and 0.5) under CMB conditions. Green, red, and blue curves indicate the densities of FeH, $FeH_{0.75}$, and $FeH_{0.5}$, respectively. Solid, dashed, and dotted curves indicate the density at different temperatures of 3000, 2500, and 2000 K. The thick solid black curve is the density of PREM [35]. The yellow region indicates the lowermost mantle, and the cyan region indicates the topmost outer core.

Fig. 4. Calculated melting temperature of fcc FeH and $FeH_{0.5}$ in comparison with the melting curves of other Fe alloys. The melting temperatures of FeH (solid) and $FeH_{0.5}$ (empty) are bracketed by triangle symbols, and up (black) and down (red) triangles denote the solid and liquid states after the simulations, respectively (Fig. S8 and S9 online). The melting curves of other Fe alloys [45,60-66] are shown with different colors. The black arrow denotes the pressure of the CMB. Updown arrows represent the estimated CMB temperature range (T_{CMB}) from previous studies [60-64,67]. The red, blue, and green arrows present the T_{CMB} estimated by the melting curves of hcp-Fe (high) [60,63,64], hcp-Fe (low) [60,61], and hcp-$Fe_{0.9}Ni_{0.1}$ accounting for the reduction due to the presence of light elements (S, O, and Si) [62]. The purple updown arrow denotes the low T_{CMB} deduced from the solidus temperature of pyrolite [67].

Fig. 5. The trajectories of H-ions in the two-phase AIMD simulation. The trajectories of individual H-ions are shown with different pink, cyan, and purple spheres. The sublattice of Fe is shown with brown spheres, and the averaged H-ion trajectory is exhibited with small light pink spheres. The trajectories for individual H-ions in both solid and liquid phases indicate H-ion interdiffusion between the solid and liquid phases.

Fig. 6. Hydrogen and water transportation in Earth's interior. The dehydration of hydrous minerals from subducted slabs generates water in the mantle. Water can react with Fe (black triangles) in the mantle or the core to form FeH (blue triangle). The accommodation of ORP above the CMB is shown with blue solid circles. The transportation of hydrogen and water is shown with green and blue arrows. The magenta numbers display the reactions between iron and water at different depths.

Yu He is a staff scientist at Key Laboratory of High-temperature and High-pressure Study of the Earth's Interior, Institute of Geochemistry, Chinese Academy of Sciences (CAS). He received his Ph.D. degree in 2012 from Institute of Physics, CAS. His research interest focuses on solid state ionics in Earth's interior. He found Earth's inner core is not a normal solid but a superionic state combination of solid iron and liquid-like carbon, oxygen, and hydrogen.

Duck Young Kim is a staff scientist at Center for High Pressure Science and Technology Advanced Research (HPSTAR), Shanghai China. He is working in computational condensed matter physics and geophysics. His research interest covers low dimensional materials, hydrous materials at deep Earth's conditions, and novel materials at multi extreme conditions

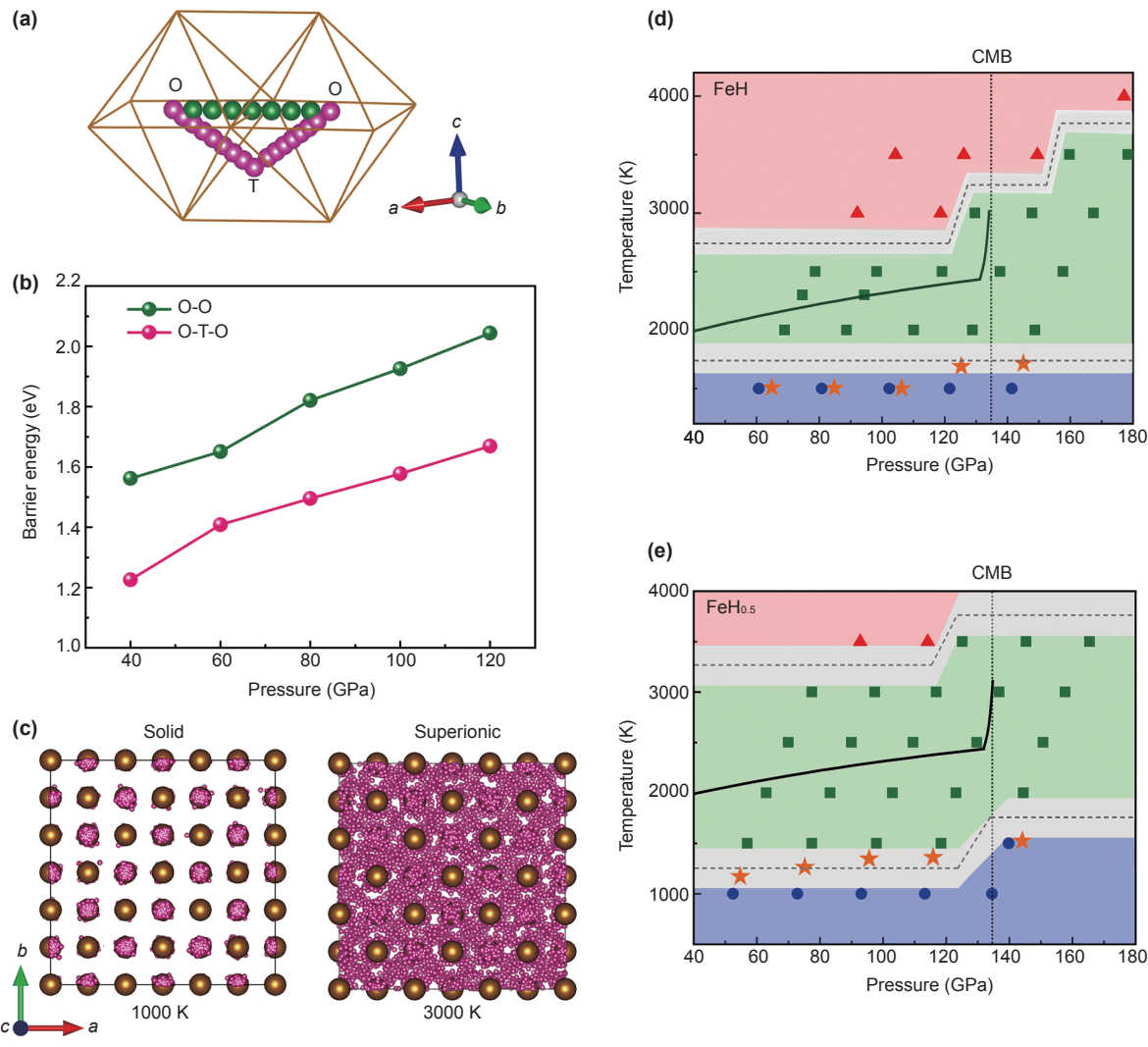
(a)
O
O
T
c
a
b
(b)
O-O
O-T-O
Barrier energy (eV)
Pressure (GPa)
(c)
Solid
Superionic
b
c
a
1000 K
3000 K
(d)
CMB
FeH
Temperature (K)
Pressure (GPa)
(e)
CMB
FeH0.5
Temperature (K)
Pressure (GPa)

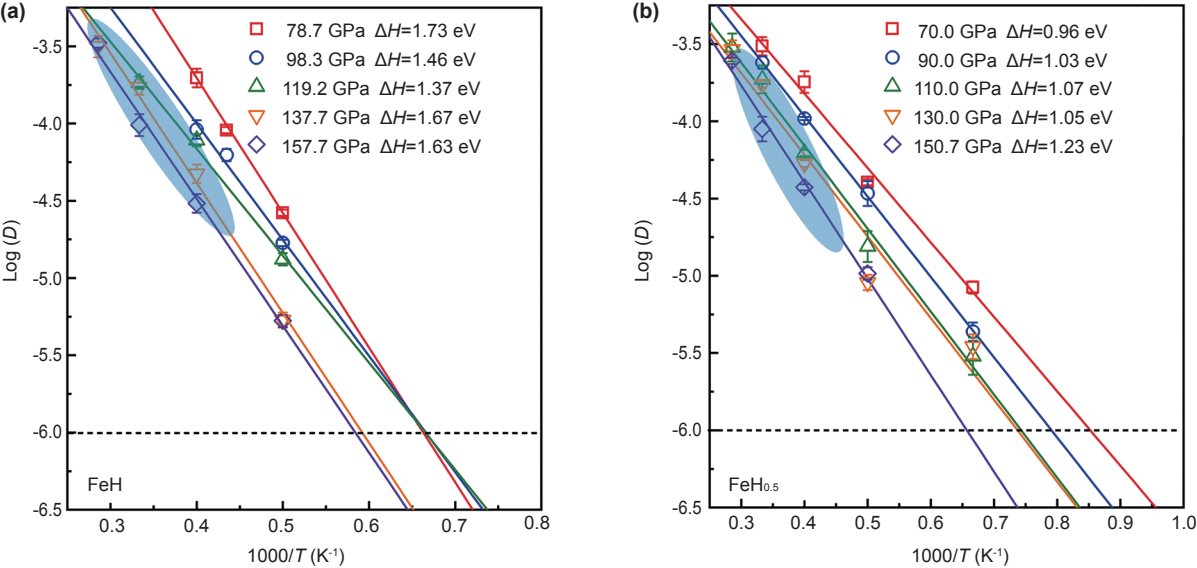
(a)
78.7 GPa ΔH=1.73 eV
98.3 GPa ΔH=1.46 eV
119.2 GPa ΔH=1.37 eV
137.7 GPa ΔH=1.67 eV
157.7 GPa ΔH=1.63 eV
FeH
Log (D)
1000/T (K-1)
-3.5
-4.0
-4.5
-5.0
-5.5
-6.0
-6.5
0.3
0.4
0.5
0.6
0.7
0.8
(b)
70.0 GPa ΔH=0.96 eV
90.0 GPa ΔH=1.03 eV
110.0 GPa ΔH=1.07 eV
130.0 GPa ΔH=1.05 eV
150.7 GPa ΔH=1.23 eV
FeH0.5
Log (D)
1000/T (K-1)
0.9
1.0

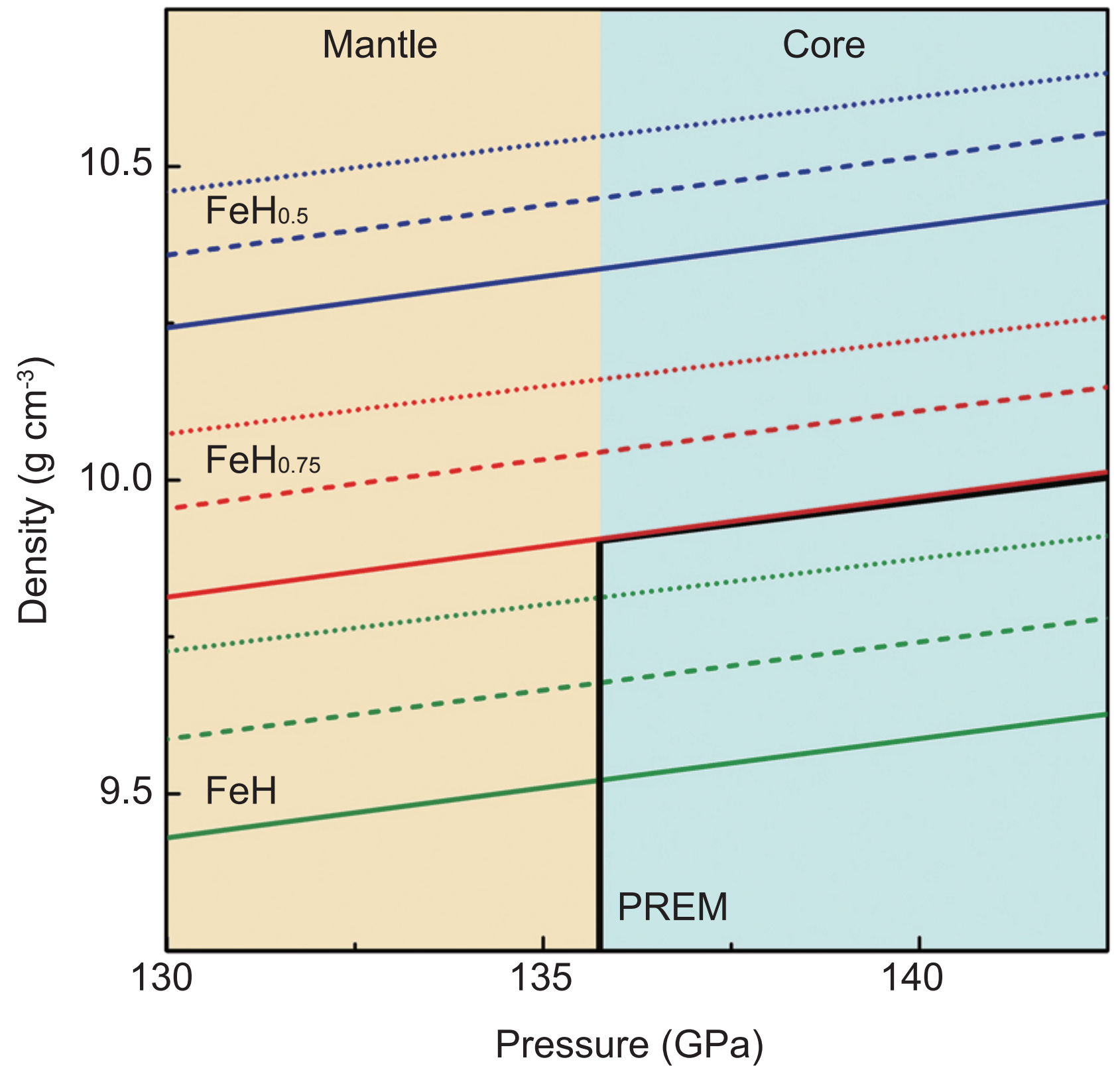
Mantle
Core
10.5
10.0
9.5
FeH0.5
FeH0.75
FeH
PREM
130
135
140
Density (g cm-3)
Pressure (GPa)

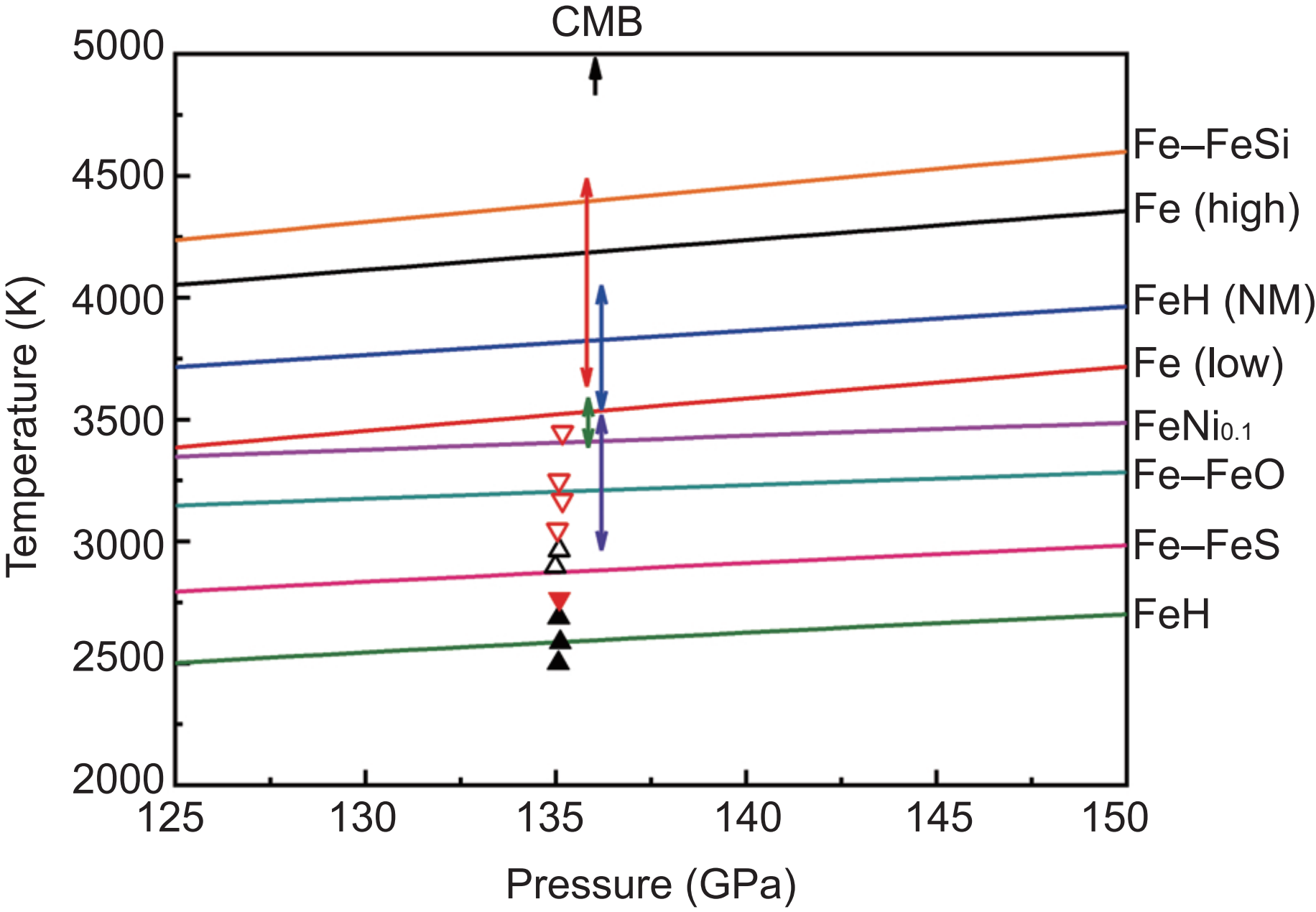
CMB
5000
4500
4000
3500
3000
2500
2000
Temperature (K)
125
130
135
140
145
150
Pressure (GPa)
Fe–FeSi
Fe (high)
FeH (NM)
Fe (low)
FeNi0.1
Fe–FeO
Fe–FeS
FeH

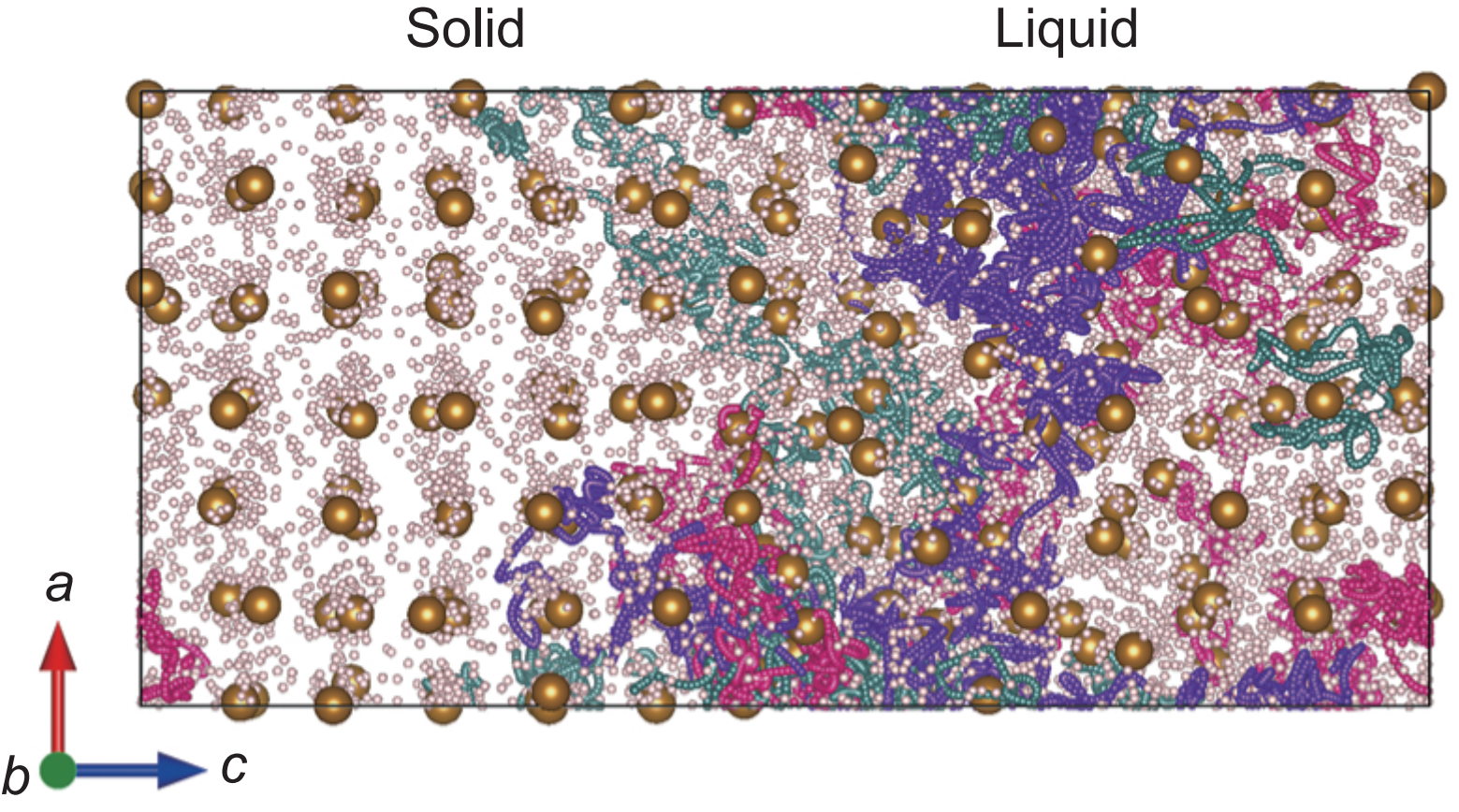
Solid
Liquid
a
b
c

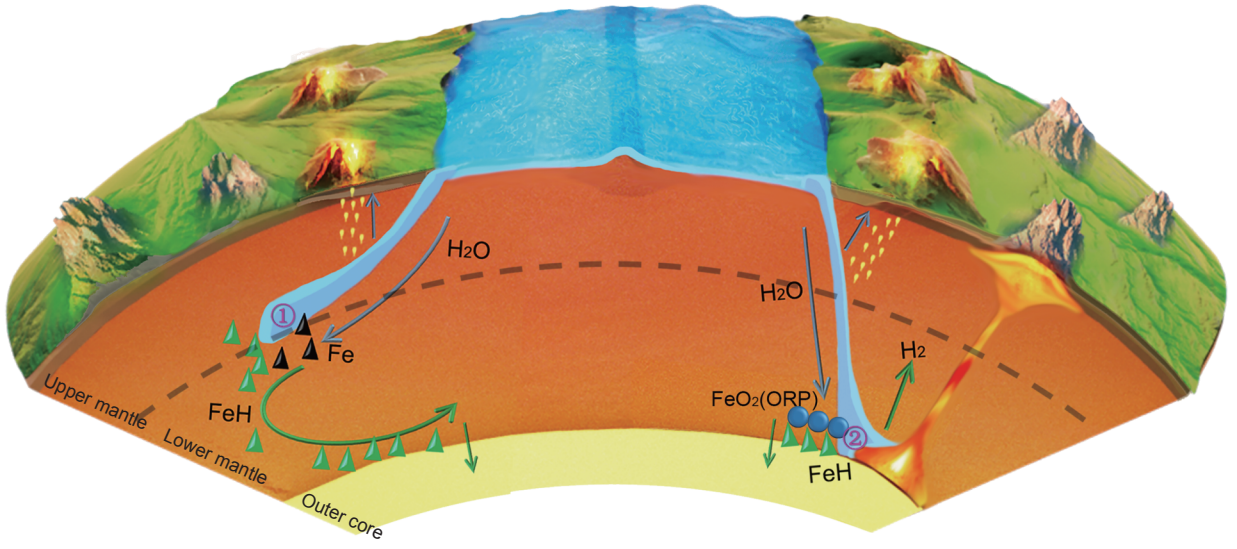
H2O
①
Fe
FeH
Upper mantle
Lower mantle
Outer core
H2O
H2
FeO2(ORP)
②
FeH